The Astrophysical Journal, 870:102 (11pp), 2019 January 10 https://doi.org/10.3847/1538-4357/aaf381

Measurements of Tropospheric Ice Clouds with a Ground-based CMB Polarization Experiment, POLARBEAR

S. Takakura[1], M. A. O. Aguilar-Faúndez[2,3], Y. Akiba[4], K. Arnold[5], C. Baccigalupi[6,7], D. Barron[8], D. Beck[9], F. Bianchini[10], D. Boettger[11], J. Borrill[12,13], K. Cheung[14], Y. Chinone[14,1], T. Elleflot[5], J. Errard[9], G. Fabbian[15], C. Feng[16], N. Goeckner-Wald[14], T. Hamada[17], M. Hasegawa[18], M. Hazumi[18,4,1,19], L. Howe[5], D. Kaneko[1], N. Katayama[1], B. Keating[5], R. Keskitalo[12,13], T. Kisner[12,13], N. Krachmalnicoff[6], A. Kusaka[20,21], A. T. Lee[14,20], L. N. Lowry[5], F. T. Matsuda[1], A. J. May[22], Y. Minami[18], M. Navaroli[5], H. Nishino[18], L. Piccirillo[22], D. Poletti[6], G. Puglisi[23], C. L. Reichardt[10], Y. Segawa[4], M. Silva-Feaver[5], P. Siritanasak[5], A. Suzuki[20], O. Tajima[24], S. Takatori[18], D. Tanabe[4], G. P. Teply[5], and C. Tsai[5]
[1] Kavli IPMU (WPI), UTIAS, The University of Tokyo, Kashiwa, Chiba 277-8583, Japan; satoru.takakura@ipmu.jp
[2] Departamento de Física, FCFM, Universidad de Chile, Blanco Encalada 2008, Santiago, Chile
[3] Department of Physics and Astronomy, Johns Hopkins University, Baltimore, MD 21218, USA
[4] Department of Particle and Nuclear Physics, SOKENDAI, Hayama, Kanagawa 240-0193, Japan
[5] Department of Physics, University of California, San Diego, CA 92093-0424, USA
[6] International School for Advanced Studies (SISSA), Via Bonomea 265, I-34136 Trieste, Italy
[7] The National Institute for Nuclear Physics, INFN, Sezione di Trieste, Via Valerio 2, I-34127 Trieste, Italy
[8] Department of Physics and Astronomy, University of New Mexico, Albuquerque, NM 87131, USA
[9] AstroParticule et Cosmologie (APC), Univ. Paris Diderot, CNRS/IN2P3, CEA/Irfu, Obs. de Paris, Sorbonne Paris Cité, France
[10] School of Physics, University of Melbourne, Parkville, VIC 3010, Australia
[11] Instituto de Astrofísica and Centro de Astro-Ingeniería, Facultad de Física, Pontificia Universidad Católica de Chile, Vicuña Mackenna 4860, 7820436 Macul, Santiago, Chile
[12] Computational Cosmology Center, Lawrence Berkeley National Laboratory, Berkeley, CA 94720, USA
[13] Space Sciences Laboratory, University of California, Berkeley, CA 94720, USA
[14] Department of Physics, University of California, Berkeley, CA 94720, USA
[15] Institut d'Astrophysique Spatiale, CNRS (UMR 8617), Univ. Paris-Sud, Université Paris-Saclay, bât. 121, F-91405 Orsay, France
[16] Department of Physics, University of Illinois at Urbana-Champaign, Urbana, IL 61801, USA
[17] Astronomical Institute, Graduate School of Science, Tohoku University, Sendai, Miyagi 980-8578, Japan
[18] Institute of Particle and Nuclear Studies, High Energy Accelerator Research Organization (KEK), Tsukuba, Ibaraki 305-0801, Japan
[19] Institute of Space and Astronautical Science, Japan Aerospace Exploration Agency (JAXA), Sagamihara, Kanagawa 252-0222, Japan
[20] Physics Division, Lawrence Berkeley National Laboratory, Berkeley, CA 94720, USA
[21] Department of Physics, The University of Tokyo, Bunkyo-ku, Tokyo 113-0033, Japan
[22] Jodrell Bank Centre for Astrophysics, University of Manchester, Manchester M13 9PL, UK
[23] Department of Physics and KIPAC, Stanford University, Stanford, CA 94305, USA
[24] Department of Physics, Kyoto University, Kyoto 606-8502, Japan
Received 2018 September 18; revised 2018 November 16; accepted 2018 November 20; published 2019 January 14

Abstract

The polarization of the atmosphere has been a long-standing concern for ground-based experiments targeting cosmic microwave background (CMB) polarization. Ice crystals in upper tropospheric clouds scatter thermal radiation from the ground and produce a horizontally polarized signal. We report a detailed analysis of the cloud signal using a ground-based CMB experiment, POLARBEAR, located at the Atacama desert in Chile and observing at 150 GHz. We observe horizontally polarized temporal increases of low-frequency fluctuations ("polarized bursts," hereafter) of $\lesssim$0.1 K when clouds appear in a webcam monitoring the telescope and the sky. The hypothesis of no correlation between polarized bursts and clouds is rejected with $>24\sigma$ statistical significance using three years of data. We consider many other possibilities including instrumental and environmental effects, and find no reasons other than clouds that can explain the data better. We also discuss the impact of the cloud polarization on future ground-based CMB polarization experiments.

Key words: atmospheric effects – scattering – cosmology: observations – cosmic background radiation – polarization

1. Introduction

The atmosphere is an unavoidable foreground in any measurement with a ground-based telescope. Absorption, emission, and scattering by atmospheric molecules define the exploitable wavelength windows for astronomical observations. In addition, turbulence in the troposphere due to convective heat transfer causes variable weather conditions and reduces the observing efficiency.

In particular, cosmic microwave background (CMB) experiments observe the sky for thousands of hours to measure very faint anisotropies from the early universe, such as degree-scale parity-odd (*B*-mode) polarization anisotropies generated by primordial gravitational waves (Seljak & Zaldarriaga 1997). Atmospheric fluctuations introduce gradually varying (low-frequency) noise and degrade the CMB anisotropy measurements at large angular scales (Lay & Halverson 2000). Therefore, the polarization of the atmosphere is a very significant concern for current and future ground-based CMB experiments.

Under a cloudless sky, the atmospheric transmission windows for CMB observation are typically the bands at <50, 70–110, 120–180, and 190–320 GHz. The atmospheric emission in this frequency range is dominated by oxygen and water vapor (e.g., Westwater et al. 2004). Fortunately, the emission is almost completely unpolarized (Kusaka et al. 2014; Errard et al. 2015), or

slightly circularly polarized because of Zeeman splitting due to the Earth's magnetic field (Rosenkranz & Staelin 1988; Keating et al. 1998; Hanany & Rosenkranz 2003; Spinelli et al. 2011). Although fluctuations in density and temperature in the turbulent atmosphere cause significant low-frequency noise for measurements of CMB intensity (or temperature), they do not affect measurements of linear polarization if the instrumental polarization leakage is negligible.

However, clouds in the atmosphere could produce linearly polarized microwave radiation. Clouds consist of small ice crystals, water droplets, or both depending on atmospheric conditions, and these small particles scatter the upwelling thermal radiation. The scattered light appears as a horizontally polarized signal in the line of sight (Troitsky & Osharin 2000; Pietranera et al. 2007). Furthermore, the horizontal alignment of ice crystals having a column or plate shape (Ono 1969; Chepfer 1999) increases the polarization signal (Czekala 1998). This linearly polarized signal from anisotropic clouds is a source of low-frequency noise for linear polarization data. It cannot be mitigated even with ideal instruments or by other techniques such as polarization modulation (Brown et al. 2009).

The impact of the polarized signal from clouds on CMB polarization measurements is fully discussed in Pietranera et al. (2007) and partially mentioned in Kuo (2017). Measurements of the signal have been reported in the atmospheric science community using microwave radiometers (Troitsky & Osharin 2000; Troitsky et al. 2003, 2005; Kneifel et al. 2010; Xie et al. 2012, 2015; Defer et al. 2014; Pettersen et al. 2016; Gong & Wu 2017). In the CMB community, the BICEP2 Collaboration et al. (2014) mention the possibility of low-frequency noise ($1/f$ noise) from clouds, and the Atacama B-mode Search (Kusaka et al. 2018) reports the existence of noise flare-ups in the polarization signal.

In this paper, we report measurements of the polarization of clouds at POLARBEAR, a ground-based experiment observing CMB polarization at 150 GHz from the Atacama Desert in Chile. To our knowledge, this is the first detailed report of this kind of effect using a CMB instrument. One of the unique features of POLARBEAR is polarization modulation using a continuously rotating half-wave plate (CRHWP) (Hill et al. 2016; Takakura et al. 2017). This technique mitigates the spurious polarization due to the leakage of unpolarized signals and instrumental temperature variations, and we can clearly measure the polarization from the sky.

In Section 2, we briefly explain the basics of the scattering of microwave radiation by ice crystals within the clouds. In Section 3, we show an example of polarization measurements during a cloudy day and then look for similar observations in 2.5 yr of data. Following the results, we discuss the impact of the clouds on the CMB experiments in Section 4 and summarize this study in Section 5.

2. Basics of Ice Clouds

The POLARBEAR experiment is located at the James Ax Observatory, at an altitude of 5200 m on Cerro Toco. This site, in the Atacama Desert in Northern Chile, is in one of the driest regions on the Earth (Suen et al. 2014). However, clouds still do occasionally exist there (e.g., Figure 7 of Kuo 2017). Clouds form when a moist air parcel expands adiabatically due to a rapid change in elevation and its water vapor content supersaturates. Clouds take various forms, which are typically classified into ten types depending on the atmospheric condition (e.g., Liou & Yang 2016). Since POLARBEAR does not have any dedicated instruments to monitor clouds, we cannot characterize them by ourselves. Here, we follow Erasmus & Van Staden (2001) and assume that the clouds at the POLARBEAR site are mostly high clouds (cirrus, cirrocumulus, and cirrostratus), which form at altitudes around 5000–13,000 m above sea level. The type of clouds will affect the amplitude and polarization fraction of the scattered radiation explained below. In this study, however, we focus on testing just the existence of the polarized signal from clouds, and the evaluation of the cloud properties is beyond our scope. The cloud type is not very important for that purpose.

The high clouds consist mainly of ice crystals,[25] which have various properties depending on the atmospheric conditions, i.e., temperature and water vapor content, as well as the evolution of the clouds. The mean effective size of an ice crystal is typically $D_e \simeq 20$–$100\ \mu$m. The ice water content (IWC), which is the density of ice in the clouds, is about 10^{-3}–10^{-1} g m^{-3} (Rolland et al. 2000). This results in a number density n of about 10^4–10^5 m^{-3}. The ice water path (IWP), which is the total mass of ice crystals per unit area, is about 1–10 g m^{-2} (Kuo 2017). Thus the geometric thickness of the cirrus clouds Δh is about 10^3 m. To be precise, the thickness ranges typically from 0.5×10^3 to 7×10^3 m, but the impact of this variation is very small in our rough estimation of the cloud signal in Section 2.1.

Ice crystals in clouds are not spherical. Small, primary crystals take the form of a hexagonal column and evolve to longer columns, larger hexagonal plates, or their aggregates depending on the temperature and humidity (Magono & Lee 1966). The aspherical shapes could cause alignment of the ice crystals due to the drag of the atmosphere (Ono 1969). One can see the signal as characteristic halos such as sundogs, circumzenithal/circumhorizontal arcs, and upper/lower tangent arcs (Cowley & Schroeder 2009).

2.1. Rayleigh Scattering

Since the size of ice crystals is sufficiently smaller than the wavelength, the scattering of microwave radiation by ice crystals is described by Rayleigh scattering. The electric field $\boldsymbol{E}_{\rm sc}$ scattered by an ice crystal located at the origin is expressed as (e.g., Landau & Lifshitz 1960)

$$\boldsymbol{E}_{\rm sc}(r\hat{\boldsymbol{n}}) = -\frac{\omega^2}{c^2 r}\hat{\boldsymbol{n}} \times (\hat{\boldsymbol{n}} \times \boldsymbol{P}), \tag{1}$$

where r is the distance from the origin, $\hat{\boldsymbol{n}}$ is a unit vector toward the propagation direction, ω is the angular frequency of the wave, and c is the speed of light. In general, the electric dipole moment $\boldsymbol{P}$ is expressed as

$$\boldsymbol{P} = V\boldsymbol{\alpha}\boldsymbol{E}_{\rm in}, \tag{2}$$

where V is the volume of the scatterer, $\boldsymbol{E}_{\rm in}$ is the incident electric field, and $\boldsymbol{\alpha}$ is the polarizability matrix, calculated as

$$\boldsymbol{\alpha} = \frac{\epsilon - 1}{4\pi}[\mathbf{I} + (\epsilon - 1)\boldsymbol{\Delta}]^{-1}, \tag{3}$$

where $\mathbf{I}$ is the identity matrix and $\boldsymbol{\Delta}$ is the depolarization factor, which is a positive definite symmetric matrix satisfying

[25] We focus on ice clouds in this study, but the same model with different parameters can be applied to clouds that consist of water droplets. Since the water droplets are spherical and more absorptive than ice, the polarization fraction would be small.

$\mathrm{Tr}(\mathbf{\Delta}) = 1$ and depending on the shape and orientation of the scatterer. In the case of spheroids, $\mathbf{\Delta}$ is parameterized as a diagonal matrix $\mathrm{diag}\{(1-\Delta_z)/2, (1-\Delta_z)/2, \Delta_z\}$, where $\Delta_z < 1/3$, $\Delta_z = 1/3$, and $\Delta_z > 1/3$ correspond to the prolate (column), spherical, and oblate (plate) shapes, respectively. The relative permittivity ϵ of ice is about 3.15 for microwave radiation (Warren & Brandt 2008).

In the simple case of spherical particles, we can obtain the total cross section of the Rayleigh scattering σ_R as

$$\sigma_R = \frac{8\pi}{3}\frac{V^2\alpha^2\omega^4}{c^4} \propto D_e^6\omega^4, \quad (4)$$

where $\alpha = (3/4\pi)(\epsilon-1)/(\epsilon+2)$. We can see the well-known dependence on the size of the scatterer D_e and the frequency of the light ω. This strong dependence on the particle size and the variation of the size distribution in clouds cause huge uncertainty in the prediction of σ_R by orders of magnitude. At the observing frequency of POLARBEAR, $\omega/(2\pi) = 150$ GHz, the cross section σ_R becomes $\sim 10^{-16}$ m^2 for $D_e = 20\,\mu$m and $\sim 10^{-12}$ m^2 for $D_e = 100\,\mu$m. By assuming that all the particles in a cloud have the same size and using the typical number density of ice crystals, $n \sim 10^4$–10^5 m^{-3}, and the typical thickness of cirrus clouds, $\Delta h \sim 10^3$ m, we estimate the optical depth of the clouds as $\tau \sim 10^{-9}$–10^{-4}. Note that the estimate increases for 220 or 280 GHz due to the frequency dependence.

The calculation above has been substantially simplified by ignoring the size and shape distributions but does indicate that larger ice crystals in clouds are the main contributor to the scattering of microwave radiation and that the optical depth would be $\lesssim 10^{-3}$ at most.

However, scattering by clouds changes the direction of the thermal radiation from the ground and injects it into the line of sight. Since almost half of the solid angle as seen from the cloud is covered by the ground at ambient temperature, scattering of the ground emission at levels below 1% could cause an additional signal at the $\sim$1 K level. The clouds are randomly distributed in the sky and are gradually varying and moving due to atmospheric turbulence and wind, which leads to low-frequency variations of the signal from the clouds. Therefore, clouds can become an important source of low-frequency noise (see Section 4 for further discussions). The cloud signal is significantly larger than the current detector noise level for CMB observations, which is lower than 1 mK over a few seconds of beam-crossing time, and thus can be detected instantaneously.

2.2. Polarization of Ice Clouds

There are mainly two types of effects that polarize the light scattered by the ice crystals. The first is due to the curvature of the ground. The second is due to the horizontal alignment of ice crystals with plate or column shape. We explain the two effects in the following. Our estimate and observation suggest the latter is dominant. Other subsidiary effects are also discussed in Section 4.3.

The three-dimensional positional relations among the telescope, the clouds, and the ground produce polarization (Figure 1). As shown in Equations (1) and (2), the polarization of the scattered light is determined by its scattering angle and the polarization of the incident light. By taking spherical coordinates (θ, ϕ) centered at the clouds and aligning the z-axis

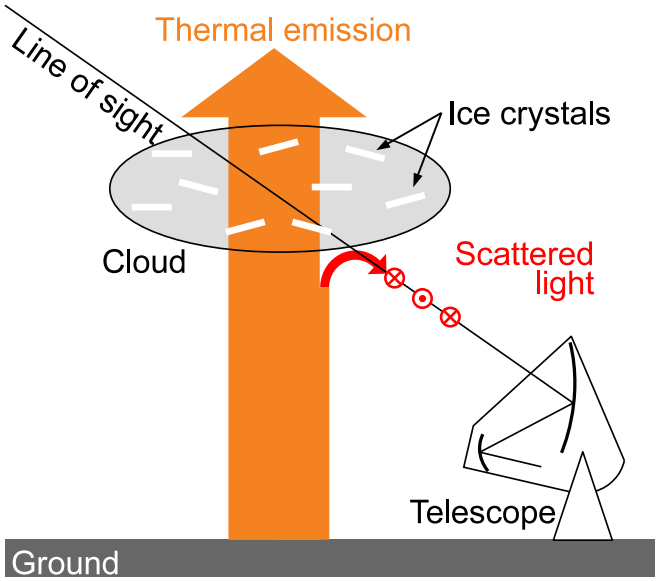

Figure 1. Illustration of the microwave signal from clouds. Ice crystals scatter thermal emission from the ground and generate horizontal polarization.

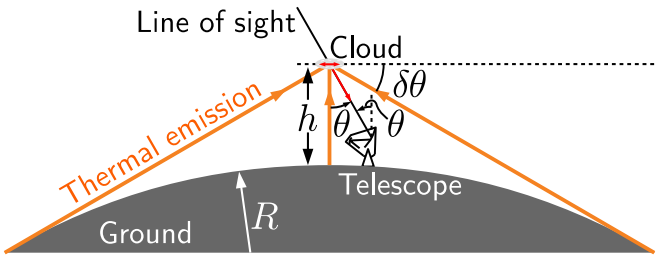

Figure 2. Sketch showing microwave radiation emitted from the spherical ground, reaching a cloud above the observing site.

to zenith as shown in Figure 2, the ground radiation can be expanded in spherical harmonics $Y_l^m(\theta, \phi)$ with $m = 0$ because of the axial symmetry. If we assume that the ground is a blackbody with a uniform temperature T_g, the expansion coefficients $a_{l,0}$ are obtained as

$$a_{l,0} = 2\pi T_g \int_0^{\frac{\pi}{2}-\delta\theta} Y_l^0(\theta, 0)\sin\theta\, d\theta. \quad (5)$$

Here, $\delta\theta$ is the look-down angle of the horizon from the clouds, which is approximately $\sqrt{2h/R}$, with the altitude of the clouds' center above sea level h and the radius of the Earth R. In particular, the monopole ($l = 0$) and quadrupole ($l = 2$) components are calculated as

$$\frac{a_{0,0}}{\sqrt{4\pi}T_g} = \frac{1-\sin\delta\theta}{2} \quad \text{and} \quad \frac{a_{2,0}}{\sqrt{4\pi}T_g} = \frac{\sqrt{5}}{4}\sin\delta\theta\cos^2\delta\theta, \quad (6)$$

respectively. Again, if we assume spherical particles to deal with the scattering simply by the optical depth τ, the Stokes parameters of the scattered light are calculated as (Hu & White 1997)

$$\begin{pmatrix} I \\ Q \end{pmatrix} \approx \frac{\tau T_g}{\sqrt{4\pi}}\begin{pmatrix} 1 \\ 0 \end{pmatrix} a_{0,0} + \frac{\tau T_g}{10}\begin{pmatrix} Y_2^0(\theta, \phi) \\ -\sqrt{6}\,{}_2Y_2^0(\theta, \phi) \end{pmatrix} a_{2,0}, \quad (7)$$

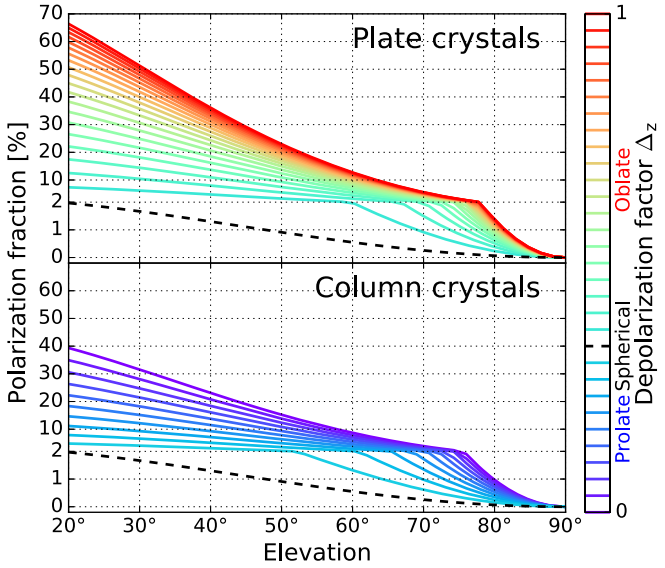

Figure 3. Calculated polarization fraction of the light scattered by horizontally aligned ice crystals with a spheroidal shape as a function of the elevation. The dashed black lines show the spherical case. The line color of the other lines represents the shape information parameterizing the z-component of the depolarization factor Δ_z. The column case shows the averaged contribution among randomly oriented particles in azimuth.

where $Y_2^0(\theta, \phi) \equiv \sqrt{5/(16\pi)}(3\cos^2\theta - 1)$, ${}_2Y_2^0(\theta, \phi) \equiv \sqrt{15/(32\pi)}\sin^2\theta$ and the other Stokes parameters, U and V, are zero. Here, the polarizations are defined on the usual base vectors ($\boldsymbol{e}_\theta$, $\boldsymbol{e}_\phi$), and the negative Stokes Q represents horizontal linear polarization. The polarization fraction p is the ratio of Q to I, thus

$$|p| \approx \frac{3}{4\sqrt{5}}\frac{a_{2,0}}{a_{0,0}}\sin^2\theta \approx \frac{3}{4}\sqrt{\frac{h}{2R}}\sin^2\theta. \quad (8)$$

Putting $h = 10$ km, $R = 6400$ km, and $\theta = 45°$ into Equation (8) results in $|p| \sim 1\%$.

Horizontally aligned ice crystals with column and plate shapes scatter horizontal electric fields more efficiently, and can therefore produce a larger polarized signal. We approximate the crystal shapes as spheroids and directly calculate Equations (1)–(3). In the case of column shape, we set the long axis horizontal but assume that its azimuth is random. The polarization fraction calculated from the model is shown in Figure 3. Here, all the crystals are assumed to have the same shape and to be horizontally aligned, i.e., the long axis of the spheroid is in the horizontal plane. Thus, these estimates give an upper limit, whereas real polarization fractions are expected to be smaller. However, the amplitude of the polarization fraction is considerably larger than the spherical case shown as the black line. This is because the horizontally aligned crystals have a tendency to scatter horizontally polarized light even without a quadrupolar anisotropy of the incident radiation field.

3. Measurements

We analyze the data taken by POLARBEAR (The POLARBEAR Collaboration et al. 2017) and search for signals that appear to be from tropospheric ice clouds. We use transition-edge sensor (TES) bolometers in the POLARBEAR receiver (Arnold et al. 2012) and a webcam monitoring the exterior of POLARBEAR and its surroundings, including the sky. Each TES bolometer is coupled to a dipole-slot antenna and measures a single polarization of the incident light. In addition, POLARBEAR has a CRHWP at the prime focus (Hill et al. 2016; Takakura et al. 2017), which is continuously rotated at 2 Hz to modulate the polarization signal from the sky. Thus, the modulated timestream of the detector $d_m(t)$ is expressed as

$$d_m(t) = I(t) + \mathrm{Re}\{[A_0 + Q(t) + iU(t)]e^{-i\omega_m t}\}, \quad (9)$$

where $I(t)$, $Q(t)$, and $U(t)$ are variations of the Stokes parameters of the sky, A_0 is the steady polarization from the instruments, and ω_m is the modulation frequency. Throughout the following analysis, the Stokes $Q(t)$ and $U(t)$ are defined on the instrumental coordinates ($\boldsymbol{e}_{ZE}$, $\boldsymbol{e}_{AZ}$), where ZE and AZ represent the zenith and azimuth angle, respectively. We demodulate the timestream and extract the polarization signal as a demodulated timestream $d_d(t)$:

$$d_d(t) = A_0 + Q(t) + iU(t). \quad (10)$$

We can also obtain the intensity signal by applying a low-pass filter. See Takakura et al. (2017) for more details. For the analysis in Section 3.1, no filters are applied anymore because the signal is very significant. For the analysis in Section 3.3, we apply the polynomial filter, the scan-synchronous signal filter, and the intensity-to-polarization leakage filter (Takakura et al. 2017) to mitigate spurious contributions such as the responsivity variation of the detectors, polarized ground signals, and instrumental polarization. For the data set used in this paper, the calibration of absolute polarization angle is still preliminary and the calibration uncertainty is about a few degrees. While further work is in progress toward the final calibration for CMB science analysis, this preliminary calibration suffices for the purpose of the study presented in this paper.

The webcam is placed in the control container located 17.2 m north of the telescope. Since it is mainly used to monitor the telescope, its field of view (FOV) covers about 130°–180° in azimuth and −10°–20° in elevation, and it takes a picture every 5 minutes.

3.1. Example

Figure 4 shows an example of the bolometer timestreams from a four-hour observation on 2014 December 18. During the observation, the telescope is azimuthally scanning the sky back and forth in an azimuth range of 133°–156° at a constant elevation of 30°. The precipitable water vapor (PWV) increases from ∼0.8 mm to ∼1.6 mm during the time of this data set. The PWV is provided by the APEX experiment (Güsten et al. 2006) using a commercial LHATPRO microwave radiometer (Rose et al. 2005). The APEX PWV will be partially correlated with the PWV at the POLARBEAR site 6 km away.

The intensity signal shown in the top panel is continuously fluctuating by ±3 K like a random walk, which is due to atmospheric turbulence. The Stokes Q in the middle panel, on the other hand, has negatively directed, burst-like structures, down by as much as ∼0.3 K relative to an offset $A_0 \sim 0.2$ K. The Stokes U also shown in the middle panel has much smaller variation than Q, which means that the burst-like signal is horizontally polarized. This property agrees with the expectation for the cloud signal that we described in Section 2.2.

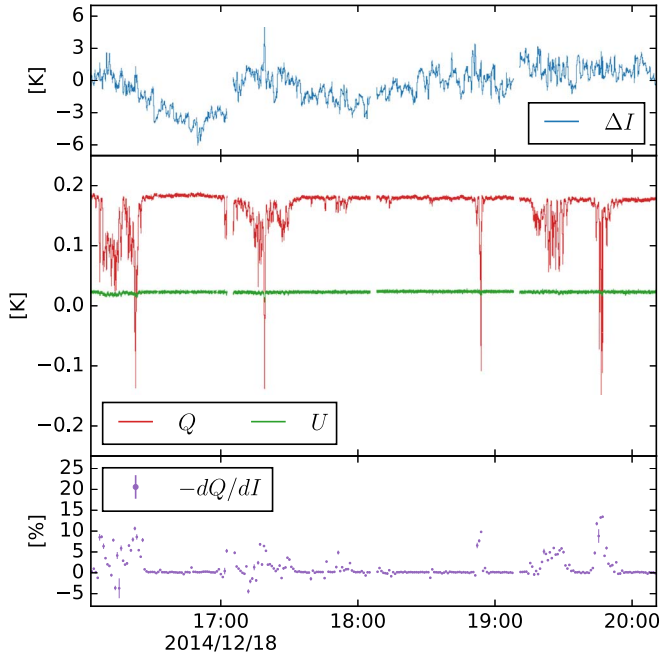

Figure 4. Example timestreams from a single bolometer during a cloudy observation. The top panel shows the Stokes I (intensity) signal, and the middle panel shows demodulated Stokes Q and U polarization signals, with the offsets due to instrumental polarization. The bottom panel shows the slope of the simple linear regression between I and Q, which corresponds to the signed Q polarization fraction.

The bottom panel shows the slope of the simple linear regression between the intensity and Q polarization signals, i.e., the signed Q polarization fraction. The intensity signal is a combination of the clouds and atmosphere, whose contributions are both a few kelvin. However, the timescale of the polarized-burst signal is shorter than that of the atmosphere. Thus, in this calculation, we apply a simple high-pass filter by subtracting the baseline for each ∼50 s one-way scan and minimize the contribution of the atmosphere. In the absence of the bursts in Q, the polarization is ∼0.1%, which is consistent with the level expected solely due to instrumental intensity-to-polarization leakage and no atmospheric polarization (Takakura et al. 2017). On the other hand, the polarization fraction significantly increases to 5%–10% at the timings of the bursts. The polarization fraction of 10% at the elevation of 30° is larger than the estimate for the spherical case in Equation (8) but can be explained by horizontally aligned column or plate crystals as shown in Figure 3.

Figure 5 is another illustration of the same data: a map of the Q polarization data as a function of the azimuth and time accompanied with snapshots from the webcam. Each horizontal row of the map corresponds to each leftward or rightward scan, which takes 50 s. Around the time of 19:45:05, there is a structure within the row, which means that the variation of the polarized-burst signal is more rapid than the scan time. In the next two scans, the structure appears consistently but at different azimuths, which suggests that the source of the signal is moving within the scan area. The timescale of the motion is several minutes. The existence of the polarized-burst signals and their motion from right to left agree well with those of the clouds in the webcam. This result also supports the argument that the origin of the signal is a cloud. Note that the maximum elevation of the webcam FOV is 20° and it does not exactly cover the scanning elevation of 30°. However, the sizes of the clouds in the photos are sufficiently large to cover most of the sky, thus we suppose that the clouds would expand to the line of sight of the telescope.

We have considered other possibilities to create the polarized-burst signal, but none of them can explain the data as well as the clouds. Sudden variations in responsivity may couple to the steady instrumental polarization A_0 and cause apparent variations in the Q timestream. However, this cannot explain the variation of $Q(t)$ to negative values in Figure 4 because the responsivity of the TES detector does not change its sign. Besides, the $2f$ signal, which is another stable optical signal from the CRHWP, does not exhibit such variations. Variations in temperature of the primary mirror could change the instrumental polarization, but the polarization fraction of the effect is expected to be less than 0.1% (Takakura et al. 2017). The far sidelobe of the telescope may have larger polarization leakage and see the ground and another part of the sky. However, the spurious signal from the ground should stay at the same azimuth, while that from the sky should be gradual rather than burst-like fluctuations. Condensation and evaporation of water vapor on the primary mirror may also cause spurious polarization. We do not have concrete evidence to reject it, but the correlation of the polarized burst with the humidity is weaker than that with the cloud detection in Section 3.3.

3.2. Cloud Detection Using the Webcam

We analyze all of the photos from the webcam and obtain the statistics of the clouds at the POLARBEAR site, in the Atacama Desert in Chile. Note again that the FOV of the webcam covers a small fraction of the sky and that the telescope points to a sky region outside the FOV in all the observations. The webcam images are not useful during the night. We also removed the pictures taken at dawn or dusk in the following analysis because the gradient of brightness in the sky increases the false detection rate.

The basic idea of the cloud detection algorithm is to find white regions in the picture. First, we mask the telescope, mountain, and ground, and split the sky into 29 patches as shown in Figure 6. For each patch, we calculate the average red–green–blue color (R, G, B) among the pixels. Then, we convert the color into hue–saturation–value color (H, S, V), specifically (Smith 1978)

$$S = \frac{\max(R, G, B) - \min(R, G, B)}{\max(R, G, B)}, \tag{11}$$

$$V = \max(R, G, B). \tag{12}$$

We set the thresholds to detect the clouds in each patch as $S < 0.1$ and $V < 0.98$, where the former condition rejects the blue sky and the latter cuts pixels saturated by the Sun. The performance of the cloud detection is checked by eye for pictures from several days chosen randomly. The algorithm often fails to detect faint clouds as in Figure 6 but rarely make false detections, which are occasionally caused by ghost images, i.e., images that appear at spurious positions due to multiple reflections.

Figure 7 shows the rate of cloud detection for each patch, i.e., the number of shots with positive cloud detection in the patch divided by the total number of shots. Although there is a small gradient in elevation, possibly due to the difference in the

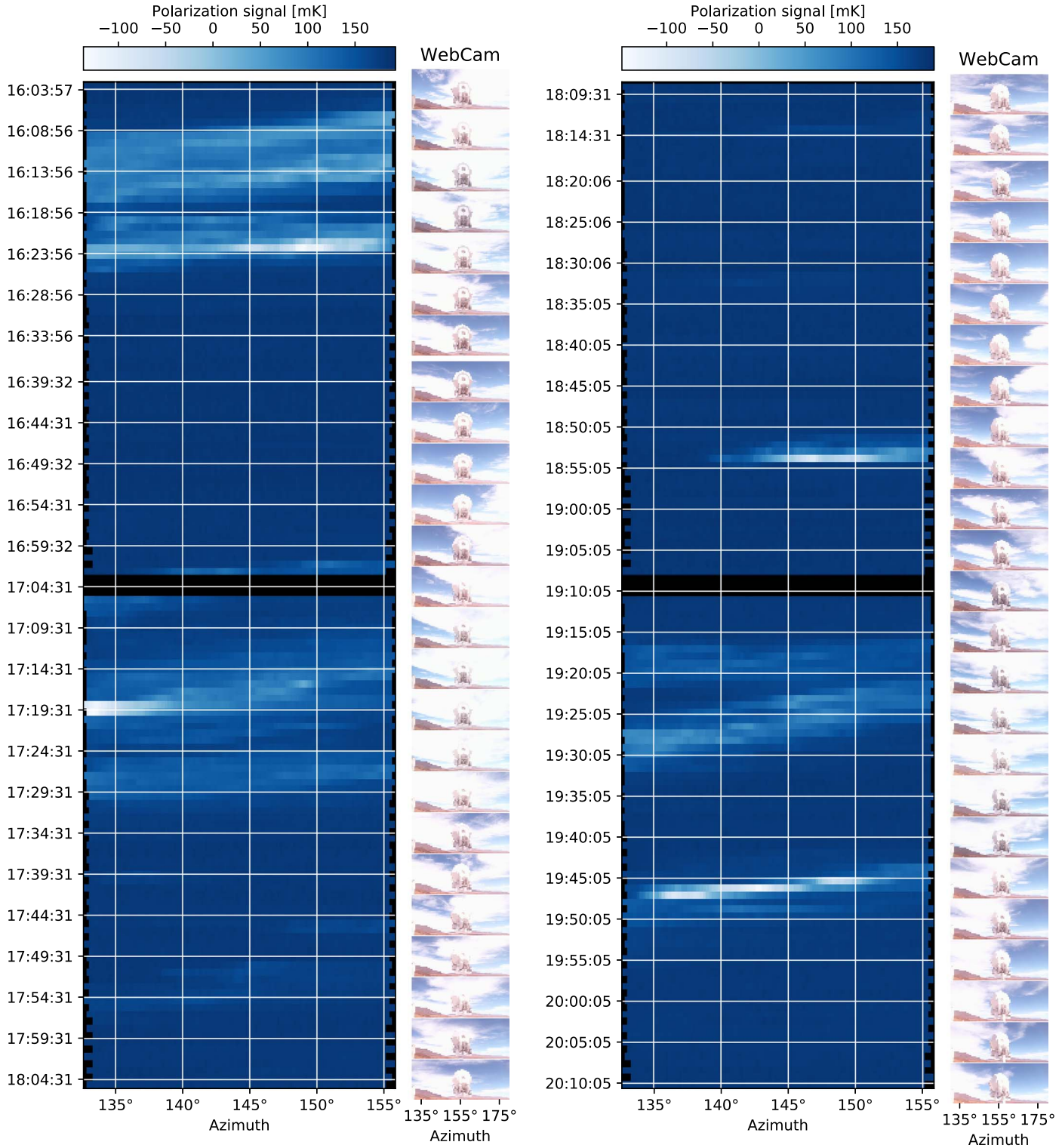

Figure 5. Comparison of the bolometer timestream with the webcam. The Stokes Q polarization timestream is mapped as a function of the azimuth ordered by time and shown as color. There are gaps to tune the instruments every hour, which are shown as black. The photos of the webcam are shown next to the map at the corresponding times. The azimuth range of the scan roughly corresponds to the left half in each of the photos. The photos show that the white clouds are carried by the wind across the sky from the right to the left. The polarized-burst signals in the map coincide with the photos with clouds and have the same trend from right to left.

area of the sky, there is no clear tendency for clouds to appear in any particular region of the FOV. The clouds may be created outside of the webcam FOV, but they are expected to persist sufficiently long enough that they will pass across the FOV.

Figures 8 and 9 show annual and daytime variations of the cloud detection rate per shot. Here we flag a shot as "cloudy" when a cloud is detected in at least one patch according to the algorithm specified above. In Figure 8, we can see the significant increase in cloud detection rate around February, which is known as Altiplanic winter (see Erasmus & Van Staden 2001 for more details about the climate of northern Chile). During that season, the cloud detection rate seems to

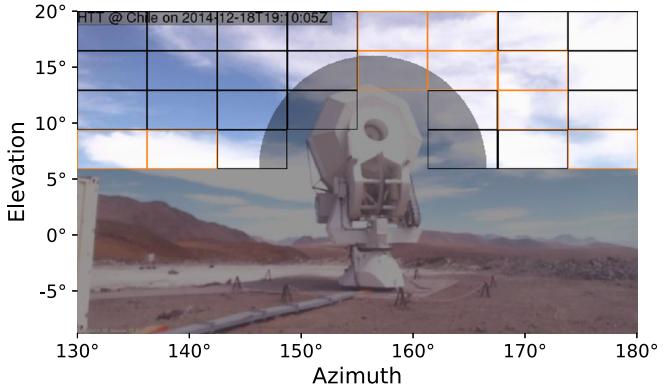

Figure 6. Example of cloud detection with a webcam image. The shadowed region shows the mask, which is fixed for all the images. The orange and black rectangles show patches with and without cloud detection in this image.

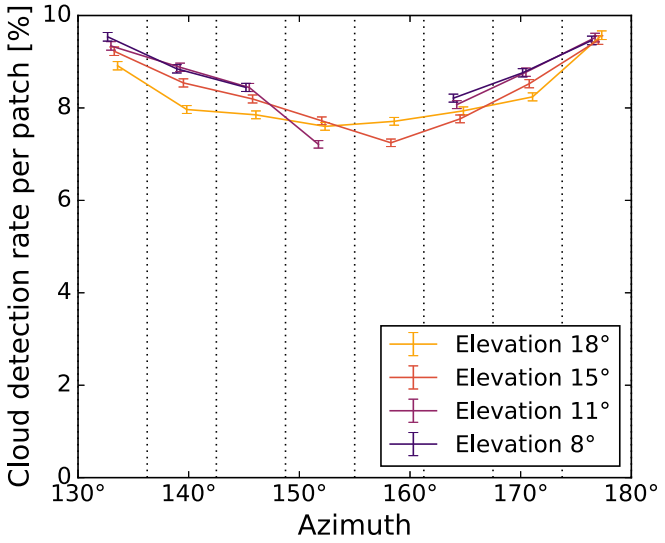

Figure 7. Cloud detection rate for each patch of the sky shown in Figure 6.

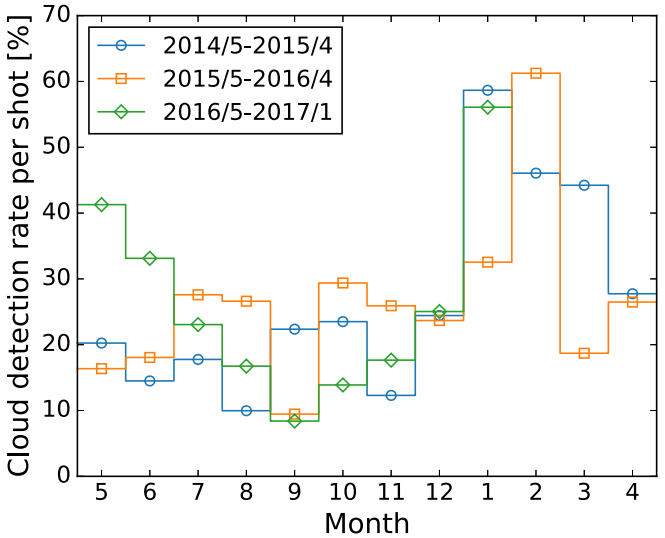

Figure 8. Annual variation of the cloud detection rate. Each line shows the result in a different year. The cloud detection rate increases in January and February every year because of Altiplanic winter.

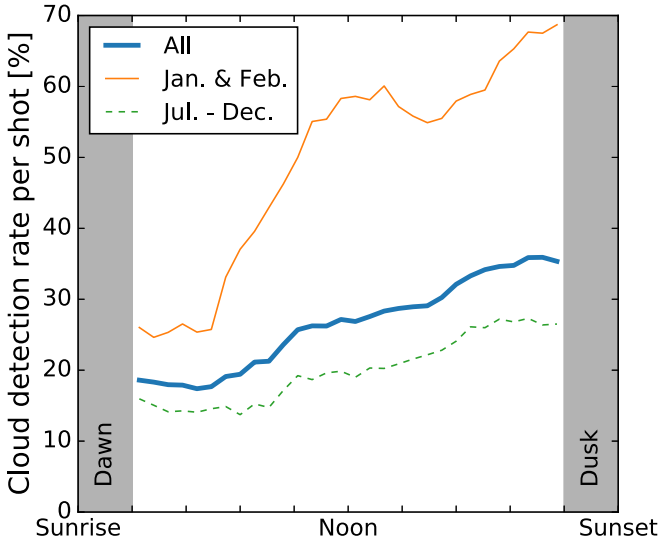

Figure 9. Daytime variation of the cloud detection rate. The horizontal axis represents the time in the daytime, which is scaled with respect to the sunrise and sunset times to adjust their seasonal variations. The blue line shows the result from all the data, and the orange and green lines show the results in the high season (January and February) and low season (from July to December), respectively. The shadowed regions show the mask used to cut dawn and dusk.

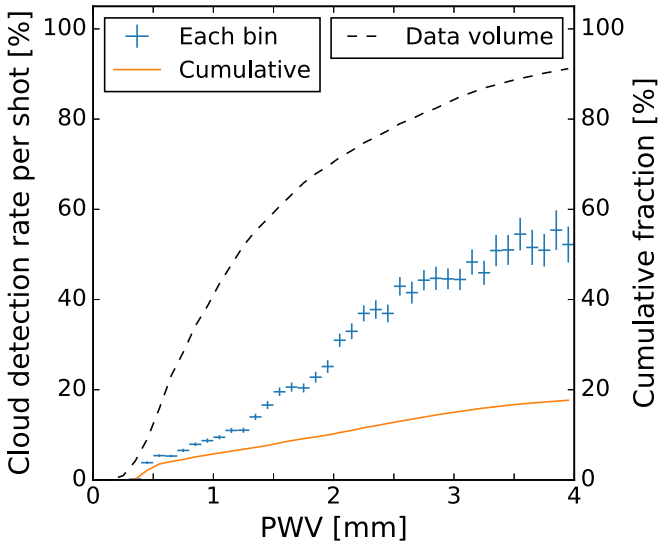

Figure 10. The dependence of the cloud detection rate on the PWV provided by the APEX experiment. Each blue point shows the rate for data in each PWV bin and the orange line shows the rate for all the data below the PWV. The cumulative fraction of the data volume is also shown as the black dashed line.

increase in the afternoon (Figure 9). It might be due to the lift of the atmosphere heated up by thermal conduction from the ground, which is also heated by sunlight. During July through December, on the other hand, the daytime trend is moderate.

Figure 10 shows the correlation between the cloud detection rate per shot and the APEX PWV. There is a clear correlation between the cloud detection and PWV. This is an expected trend and provides additional support and validation to our cloud detection method.

The overall cloud detection rate per shot is about 26%. Note that we use only the daytime photos and have no information during the night.

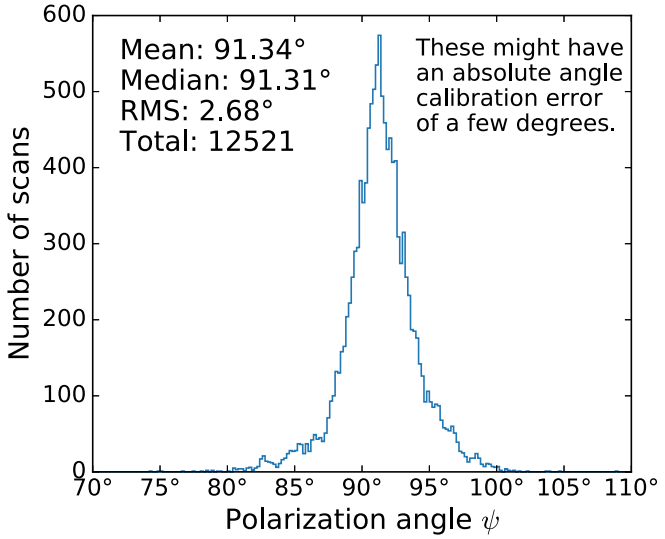

Figure 11. The histogram of the polarization angle of the polarized-burst signal ψ. The mean, median, and rms values are calculated from samples in the range of $70° < \psi < 110°$. There are no other bunches outside the range shown. Note that we have not finalized the calibration of absolute angle for this data set yet, and it might have an error of a few degrees.

3.3. Cloud Detection in the Bolometer Data

By using the polarized-burst signals in the bolometer data, we also detect clouds as shown in Figure 4. We use the POLARBEAR data from 2014 July to 2017 January. The cloud detection results are compared with the webcam study described in Section 3.2.

Since the typical size of the clouds should be larger than the FOV of POLARBEAR, 3°, the cloud signal is correlated among all the detectors. Thus, we can improve the sensitivity to detect the clouds by averaging the timestreams over all the detectors. Similar to Kusaka et al. (2014), we separate the averaged polarization timestreams, $Q(t)$ and $U(t)$, into two components using the method of principal component analysis (PCA) as

$$X_1(t) + iX_2(t) = \{Q(t) + iU(t)\}\, e^{-i\phi}, \tag{13}$$

where the rotation ϕ is determined to maximize the variance of $X_1(t)$. Since the secondary component $X_2(t)$ is dominated by the detector white noise, the signal-to-noise ratio (S/N) of the cloud is calculated as

$$\mathrm{S/N} = \sqrt{\frac{\sigma(X_1)^2}{\sigma(X_2)^2} - 1}\,, \tag{14}$$

where σ denotes the standard deviation. The polarization angle of the signal ψ is obtained as

$$\psi = \frac{\phi}{2}. \tag{15}$$

Here, we assume that the signal is almost horizontal as shown in Figure 4, and constrain $\pi/2 < \phi < 3\pi/2$, which cannot be determined by PCA due to degeneracy.

Figure 11 shows a histogram of the polarization angle of the polarized-burst signal ψ with S/N > 10 for each scan. If we have any instrumental noise sources other than the clouds, e.g., intensity leakage due to the detector nonlinearity, the polarized ground structure, and the HWP encoder error, they could appear at angles $\psi \nsim 90°$. Having only the single peak at $\psi \sim 90°$ is evidence that such extra noises are not significant and that all the polarized-burst signals are most likely coming from clouds. There are still possibilities of the responsivity variation due to electrical noise and the temperature variation of the primary mirror, but they cannot explain the coincidence with the webcam described below. Both the width of the peak, rms $= 2.^{\circ}68$, and the offset from $\psi = 90°$ might be due to a systematic error of the cloud signal or the instrument, which is still under investigation (see more discussions in Section 4.3).

Table 1
One-hour Observations Containing Polarized-burst Signals

Data	Webcam	Polarized Burst	
Daytime	All	16.1%	(295/1835)
	Cloud	46.3%	(279/602)
	No cloud	1.3%	(16/1233)
Night	···	9.7%	(458/4735)

Note. The table shows the fractions of the one-hour observations containing polarized-burst signals found in the bolometer data for the data sets corresponding either to a concurrent cloud detected in the webcam or to no cloud detected. The fraction of burst-like signals occurring at night is also listed, though clouds cannot be identified by the webcam during the night. The original numbers of one-hour observations are shown in parentheses.

Each of the CMB observations typically takes one hour and contains 40–70 left and right scans at a constant elevation. We calculate the S/N and polarization angle ψ of the cloud signal for each scan and take the values with the highest S/N as representative of the CMB observation. On the other hand, the detection of clouds by the webcam is determined by a detection in at least one of the ∼12 photos taken during the observation. Note that the CMB observations are performed at all times of the day, but the webcam can be used during the daytime only.

Table 1 shows the coincidence of the cloud detection in the bolometer data with that in the webcam. For the data with clouds in the webcam, the rate of polarized-burst detection significantly increases to 46.3% compared to 1.3% for the data without clouds. Assuming that the appearance of polarized bursts in the bolometer data and the appearance of clouds in the webcam each occur at their observed rates but are also independent, then the significance of observing such a strong covariance between them is estimated to be $>24\sigma$. Note again that the FOV of the webcam does not cover the sky regions of the CMB observations. That could be the reason for the deviation from a perfect separation. Also, the daytime rate of polarized bursts is 16.1%, which is smaller than ∼30%, the fraction of data with clouds detected by the webcam (Section 3.2). This is because CMB observations are not performed when PWV > 4 mm, or the webcam is more sensitive to clouds than bolometers in this analysis using the thresholds above. For the night data, we have no information on the clouds from the webcam, but polarized-burst signals are detected in 9.7% of the data.

Figure 12 shows the distribution of the S/N for each data set. Note that it shows the partial data with high S/N (Table 1). Again, it shows the clear difference between the data with and without clouds detected by the webcam. Besides, the S/N distribution for the night data is very similar to that for the daytime data with clouds. As explained in Section 2.2, the clouds scatter the thermal emission from the ground, which

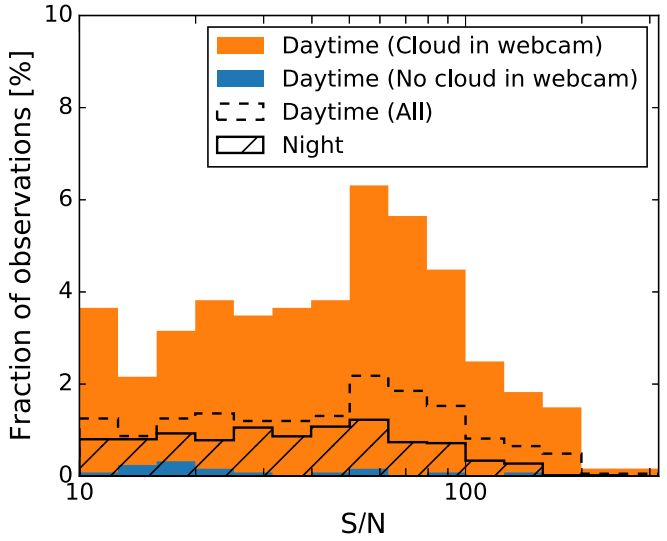

Figure 12. The histogram of the maximum S/N of the polarized-burst signal in each observation normalized by the number of observations. The orange and blue histograms show the results for the daytime data with and without clouds detected by the webcam, and the result for all the daytime data is shown as the dashed line. The result for the night data is also shown as the hatched histogram. The outliers in the blue histogram might be due to clouds outside of the webcam FOV.

also takes place at night. Our results support the expectation that the cloud signal also exists during the night.

4. Discussion

In the previous section, we have shown that the polarized cloud signals are detected in the CMB observations with POLARBEAR. Here, we discuss the impact of the clouds on CMB polarization measurements.

4.1. Degradation of the Statistical Precision

CMB measurements require thousands of hours of observations with high-sensitivity detectors to measure the faint CMB signals. The cloud signal is just noise that lowers the quality of the observations.

One simple approach to reduce the impact of the clouds is to drop noisy data, but that would inevitably reduce the observation efficiency.[26] It is possible to detect cloud signals in the bolometer data to an extent as performed in Section 3.3. We find cloud-like polarized-burst signals in 16.1% (9.7%) of one-hour observations (Table 1) and in 5.2% (3.0%) of leftward or rightward scans during the daytime (night). One could use image analysis similar to Section 3.2, in which we detect clouds in 26% of all the daytime shots of the webcam. As shown in Figure 10, the fraction of data without clouds improves if we observe only in good PWV. But this decreases the total amount of data.

Even with data cuts, we expect residuals from faint clouds below the detection threshold. These residuals will be present at low frequency with a $1/f$ behavior and degrade the detector performance at large angular scales. Such residuals cannot be mitigated by polarization modulation techniques such as the CRHWP used in POLARBEAR.

[26] Since the cloud signal only affects the Stokes Q polarization, it may be possible to save the Stokes U component.

If we detect the clouds using the bolometer data as performed in Section 3.3, the residual noise level will depend on the S/N threshold of the cloud detection. For example, to achieve an S/N of 10, the power of the cloud signal should be 100 times larger than that of the detector noise. In other words, residual $1/f$ noise below the threshold could naïvely degrade the sensitivity of the CMB angular power spectra by a factor of 100 in the worst case. Tightening the threshold will mitigate the contamination but also decrease the observation efficiency. Thus, optimization of the threshold is required to maximize performance.

The effect of clouds will depend on the telescope FOV and the detector beam size. Small-aperture telescopes with a large FOV have a high probability of seeing clouds. Large-aperture telescopes with small beams have a high instantaneous S/N of a cloud, because many detectors simultaneously observe the same cloud, which is larger than the beam size.

These studies could inform forecasting and optimization of future CMB experiments, such as CMB-S4 (Abazajian et al. 2016).

4.2. Systematic Errors on CMB Measurements

Systematic errors due to the residual cloud signal are also of concern for CMB measurements.

The cloud signal is horizontally polarized, i.e., $Q < 0$, and does not fluctuate symmetrically between positive and negative. This highly non-Gaussian fluctuation could lead to possible systematics in the map because many map-making algorithms assume Gaussianity for noise fluctuations. This systematics can be mitigated to some extent by parallactic angle rotation.

The cloud signal would affect foreground removal due to its distinct frequency dependence. By using maps at multiple frequencies, we separate the CMB and the other foregrounds that are stationary in the sky, i.e., not associated with any Earth or atmospheric motion, such as the Galactic dust and synchrotron emissions. Since the cloud signal has a Rayleigh scattering spectrum that is $\propto\omega^6$ (see Equation (4) with additional ω^2 from the spectrum of the ground emission), it would appear to rise in frequency, similar to a dust component (approximately $\omega^{1.5}$), but much more steeply. On the other hand, the atmospheric motion would likely decorrelate with astrophysical foregrounds, making control of the clouds appropriate for a time domain analysis, rather than in maps.

Clouds staying in the same position may also cause systematic errors. However, there is no significant localized cloud feature appearing in Figure 7. In addition, any localized clouds would be fixed to ground features, such as mountains, but the rotation of the sky would change the relative positions and suppress systematic errors.

The daytime trend of the cloud detection rate shown in Figure 9 might cause a systematic difference in the additional noise from the residual cloud signals between the morning and afternoon observations. However, the yearly motion of the Earth gradually shifts the observing time of the CMB patch fixed on the sky. For year-long observations, the difference will be at least partially averaged.

Performing null tests sensitive to the clouds is necessary to validate the data. A split of rising versus setting can test for localized clouds, and a split of summer versus winter can test the impact of the diurnal variation as mentioned above. A split

of low-PWV versus high-PWV can test the cloud rate because of their correlation as shown in Figure 10.

4.3. Polarization Angle Calibration

While ice clouds are a nuisance in CMB observations, the polarized signal from the clouds could be a useful calibrator for the absolute polarization angle. As explained in Section 2.2 and demonstrated in Figures 4 and 11, the signal is horizontally polarized mainly because the column or plate ice crystals are aligned horizontally by gravity. The center of cirrus clouds lie at an altitude of ∼10 km above sea level, so the distance from the telescope is sufficient to achieve a far-field measurement for POLARBEAR with the 2.5 m diameter aperture observing at 150 GHz. Furthermore, the clouds are diffuse objects, making beam systematics of less concern. These two properties are better than those for near-field calibrators, such as the sparse wire grid in front of the telescope (Tajima et al. 2012; Kusaka et al. 2018), which need a connection from the near-field measurement to the far-field beam that relies on the optics model. Although the spectrum of the cloud signal depends strongly on the observing frequency as $\propto\omega^6$, the polarization angle does not depend on the frequency. This addresses an uncertain polarization angle rotation feature of Tau A, a popular polarized celestial source. Cloud calibration would make it possible to operate the detectors with typical sky loading, as opposed to extra loading when observing a source near the ground, and it would not have uncertainty in extrapolating the pointing model of the telescope.

In Figure 11, the precision of the polarization angle calibration for each scan is only $2\overset{\circ}{.}7$, but the uncertainty of the mean value can be reduced by accumulating statistics to $0\overset{\circ}{.}03$, provided the errors are independent and Gaussian distributed. That is better than the statistical uncertainty of $0\overset{\circ}{.}16$ from the polarization angle calibration from nulling the apparent correlation between the CMB *E*- and *B*-mode patterns from two years of POLARBEAR data (The POLARBEAR Collaboration et al. 2017). In addition, the cloud polarization is absolutely referenced to gravity, and it does not use assumptions about the symmetry properties of the CMB.

On the other hand, the cloud signal may have its own systematic errors. For example, wind and electrification may slightly tilt the ice crystals. The ground emission may not be uniform due to local features, e.g., deserts, mountains, lakes, snowfields, etc. The contribution of the Sun can become non-negligible. We have estimated the systematic error by splitting the data into subsets for various observation conditions: splits can be by year, day–night, scan direction, PWV, outside temperature, and wind speed. The median value for each subset has a variation of about $0\overset{\circ}{.}4$. However, that value also includes the systematic error of the instrument such as variations in the time constant value of the detector during the observation and imperfection of the pointing model. Further investigation is necessary to separate them, but the possibility of having many measurements with various conditions demonstrates the potential usefulness of the cloud signal as a calibrator of polarization angle.

4.4. Prescription for Future Experiments

For future ground-based CMB experiments aimed at more precise measurement of CMB polarization, such as the CMB-S4, steps to mitigate the contamination of the cloud signal will be necessary.

One approach is remote sensing of clouds from the ground on site. In Section 3.1, we have demonstrated a simple cloud detection technique using the webcam for monitoring the telescope. Even with the limitation of its FOV, a significant coincidence of the cloud detections between the webcam and bolometers is observed as shown in Table 1 and Figure 12. This can be improved by using a whole-sky camera and a co-mounted infrared camera, which would be useful during the night (e.g., Suganuma et al. 2007). As already mentioned by Pietranera et al. (2007), the most informative but challenging method is polarized lidar (e.g., Lewis et al. 2016), which shoots a laser pulse into the sky, receives the scattered light, and characterizes the atmospheric properties along the line of sight including the shape, size distribution, and orientation of the ice crystals. These tools would enable reliable cloud detection and precise data selection. This would also help with understanding the clouds and reducing the systematic error in polarization angle.

Another approach might be to perform foreground separation in the time domain. The clouds are obviously the frontmost component of the foregrounds for CMB observations. The cloud signal has a frequency dependence markedly different from that of the CMB and other astrophysical foregrounds, i.e., approximately ω^6 as opposed to ω^{-3} for synchrotron and $\omega^{1.5}$ for dust. Therefore, it would be possible to separate the cloud signal in measurements with multi-frequency bands. Here, it is important to observe the same position at the same time among detectors with different frequency bands. The multi-chroic detector technique used in, e.g., the Simons Array experiment (Stebor et al. 2016) would be useful for that purpose.

Of course, satellite missions are the best solution to avoid the clouds. Balloon-borne experiments may see clouds in the mesosphere, but their impact would be small because the particles in mesospheric clouds are smaller than those in tropospheric clouds.

5. Summary

The ice crystals in tropospheric clouds scatter thermal emission from the ground and produce horizontally polarized signals. In particular, column and plate crystals should have the tendency to align horizontally with respect to the ground, which enhances the polarization fraction by tens per cent.

In this study, we have presented measurements of clouds with the POLARBEAR experiment. The horizontal polarization and the significant coincidence between the detectors and webcam strongly support the argument that the polarized-burst signals are actually coming from the clouds. Note that the polarization modulation technique using the CRHWP is essential to make a clear separation between the intensity and polarization signals.

Dropping data with clouds could decrease the efficiency of CMB observations. In the webcam analysis, clouds are detected in 26% of all the daytime shots. In addition, the residual cloud signal may become a critical source of low-frequency noise and systematic error that cannot be mitigated with polarization modulation techniques. In future experiments, in situ measurements of clouds with extra instruments or a sophisticated analysis combining multi-frequency detectors will help mitigate the contamination.

On the other hand, the cloud signal could potentially be a good calibrator of the absolute polarization angle with $0\overset{\circ}{.}03$

precision if the systematic errors of 0°.4 associated with it can be understood.

S. Takakura was supported by Grant-in-Aid for JSPS Research Fellow JP14J01662 and JP18J02133. The POLARBEAR project is funded by the National Science Foundation under Grants No. AST-0618398 and No. AST-1212230. The James Ax Observatory operates in the Parque Astronómico Atacama in northern Chile under the auspices of the Comisión Nacional de Investigación Científica y Tecnológica de Chile (CONICYT). The APEX PWV was obtained from the APEX Weather Query Form of the ESO Science Archive Facility. This research used resources of the Central Computing System, owned and operated by the Computing Research Center at KEK, the HPCI system (Project ID:hp150132), and the National Energy Research Scientific Computing Center, a DOE Office of Science User Facility supported by the Office of Science of the U.S. Department of Energy under Contract No. DE-AC02-05CH11231. Kavli IPMU was supported by World Premier International Research Center Initiative (WPI), MEXT, Japan. This work was supported by MEXT KAKENHI grant No. 21111002, JP15H05891, and JP18H05539, JSPS KAKENHI grant No. JP26220709, JP26800125, and JP16K21744, and the JSPS Core-to-Core Program. M.A. acknowledges support from CONICYT UC Berkeley-Chile Seed Grant (CLAS fund) Number 77047, Fondecyt project 1130777 and 1171811, DFI postgraduate scholarship program and DFI Postgraduate Competitive Fund for Support in the Attendance to Scientific Events. C.B., N.K., and D.P. acknowledge support from the RADIOFOREGROUNDS project (radioforegrounds.eu), funded by the European Commission's H2020 Research Infrastructures under the Grant Agreement 687312, the INDARK INFN Initiative and the COSMOS network of the Italian Space Agency (cosmosnet.it). F.B. and C.R. acknowledge support from an Australian Research Council Future Fellowship (FT150100074). D. Boettger gratefully acknowledges support from grant ALMA CONICYT 31140004. G.F. acknowledges the support of the CNES postdoctoral program. Work at LBNL was supported by the Laboratory Directed Research and Development Program of Lawrence Berkeley National Laboratory under U.S. Department of Energy Contract No. DE-AC02-05CH11231. A.K. acknowledges the support by JSPS Leading Initiative for Excellent Young Researchers (LEADER). F.M. acknowledges JSPS International Research Fellowship (grant No. JP17F17025).

ORCID iDs

S. Takakura https://orcid.org/0000-0001-9461-7519
M. A. O. Aguilar-Faúndez https://orcid.org/0000-0002-1571-663X
K. Arnold https://orcid.org/0000-0002-3407-5305
D. Barron https://orcid.org/0000-0002-1623-5651
F. Bianchini https://orcid.org/0000-0003-4847-3483
Y. Chinone https://orcid.org/0000-0002-3266-857X
G. Fabbian https://orcid.org/0000-0002-3255-4695
M. Hasegawa https://orcid.org/0000-0003-1443-1082
B. Keating https://orcid.org/0000-0003-3118-5514
R. Keskitalo https://orcid.org/0000-0001-5748-5182
A. T. Lee https://orcid.org/0000-0003-3106-3218
Y. Minami https://orcid.org/0000-0003-2176-8089
H. Nishino https://orcid.org/0000-0003-0738-3369
G. Puglisi https://orcid.org/0000-0002-0689-4290
C. L. Reichardt https://orcid.org/0000-0003-2226-9169
M. Silva-Feaver https://orcid.org/0000-0001-7480-4341
P. Siritanasak https://orcid.org/0000-0001-6830-1537

References

Abazajian, K. N., Adshead, P., Ahmed, Z., et al. 2016, arXiv:1610.02743
Arnold, K., Ade, P. A. R., Anthony, A. E., et al. 2012, Proc. SPIE, 8452, 84521D
BICEP2 Collaboration, Ade, P. A. R., Aikin, R. W., et al. 2014, ApJ, 792, 62
Brown, M. L., Challinor, A., North, C. E., et al. 2009, MNRAS, 397, 634
Chepfer, H. 1999, JQSRT, 63, 521
Cowley, L., & Schroeder, M. 2009, HaloSim3 Ray Tracing Simulator, https://www.atoptics.co.uk/halosim.htm
Czekala, H. 1998, GeoRL, 25, 1669
Defer, E., Galligani, V. S., Prigent, C., & Jimenez, C. 2014, JGRD, 119, 12
Erasmus, D. A., & Van Staden, C. A. 2001, Cerro Tololo Inter-American Observatory, http://www.eso.org/gen-fac/pubs/astclim/forecast/erasmus/Erasmus_N-Chile-APR2001.pdf
Errard, J., Ade, P. A. R., Akiba, Y., et al. 2015, ApJ, 809, 63
Gong, J., & Wu, D. L. 2017, ACP, 17, 2741
Güsten, R., Nyman, L. Å, Schilke, P., et al. 2006, A&A, 454, L13
Hanany, S., & Rosenkranz, P. 2003, NewAR, 47, 1159
Hill, C. A., Beckman, S., Chinone, Y., et al. 2016, Proc. SPIE, 9914, 99142U
Hu, W., & White, M. 1997, PhRvD, 56, 596
Keating, B., Timbie, P., Polnarev, A., & Steinberger, J. 1998, ApJ, 495, 580
Kneifel, S., LöHnert, U., Battaglia, A., Crewell, S., & Siebler, D. 2010, JGRD, 115, D16214
Kuo, C.-L. 2017, ApJ, 848, 64
Kusaka, A., Appel, J., Essinger-Hileman, T., et al. 2018, JCAP, 2018, 005
Kusaka, A., Essinger-Hileman, T., Appel, J. W., et al. 2014, RScI, 85, 024501
Landau, L. D., & Lifshitz, E. M. 1960, The Electrodynamics of Continuous Media (Oxford: Pergamon)
Lay, O. P., & Halverson, N. W. 2000, ApJ, 543, 787
Lewis, J. R., Campbell, J. R., Welton, E. J., Stewart, S. A., & Haftings, P. C. 2016, JAtOT, 33, 2113
Liou, K.-N., & Yang, P. 2016, Light Scattering by Ice Crystals: Fundamentals and Applications (Cambridge: Cambridge Univ. Press)
Magono, C., & Lee, C. W. 1966, J. Fac. Sci. Hokkaido Univ., 2, 321
Ono, A. 1969, JAtS, 26, 138
Pettersen, C., Bennartz, R., Kulie, M. S., et al. 2016, ACP, 16, 4743
Pietranera, L., Buehler, S. A., Calisse, P. G., et al. 2007, MNRAS, 376, 645
Rolland, P., Liou, K. N., King, M. D., Tsay, S. C., & McFarquhar, G. M. 2000, JGR, 105, 11
Rose, T., Crewell, S., Löhnert, U., & Simmer, C. 2005, AtmRe, 75, 183
Rosenkranz, P. W., & Staelin, D. H. 1988, RaSc, 23, 721
Seljak, U., & Zaldarriaga, M. 1997, PhRvL, 78, 2054
Smith, A. R. 1978, SIGGRAPH Comput. Graph., 12, 12
Spinelli, S., Fabbian, G., Tartari, A., Zannoni, M., & Gervasi, M. 2011, MNRAS, 414, 3272
Stebor, N., Ade, P., Akiba, Y., et al. 2016, Proc. SPIE, 9914, 99141H
Suen, J. Y., Fang, M. T., & Lubin, P. M. 2014, ITTST, 4, 86
Suganuma, M., Kobayashi, Y., Okada, N., et al. 2007, PASP, 119, 567
Tajima, O., Nguyen, H., Bischoff, C., et al. 2012, JLTP, 167, 936
Takakura, S., Aguilar, M., Akiba, Y., et al. 2017, JCAP, 2017, 008
The POLARBEAR Collaboration, Ade, P. A. R., Aguilar, M., et al. 2017, ApJ, 848, 121
Troitsky, A. V., & Osharin, A. M. 2000, R&QE, 43, 356
Troitsky, A. V., Osharin, A. M., Korolev, A. V., & Strapp, J. W. 2003, JAtS, 60, 1608
Troitsky, A. V., Vostokov, A. V., & Osharin, A. M. 2005, R&QE, 48, 281
Warren, S. G., & Brandt, R. E. 2008, JGRD, 113, D14220
Westwater, E. R., Crewell, S., & Matzler, C. 2004, URSI Radio Science Bulletin, 2004, 59
Xie, X., Crewell, S., Löhnert, U., Simmer, C., & Miao, J. 2015, JGRD, 120, 6145
Xie, X., LöHnert, U., Kneifel, S., & Crewell, S. 2012, JGRD, 117, D02206